

## Computer Simulation of the Tension of Noncrystalline Silicon Nanoparticles

A. E. Galashev<sup>a</sup>, I. A. Izmodenov<sup>b</sup>, O. R. Rakhmanova<sup>b</sup>, and O. A. Novruzova<sup>b</sup>

<sup>a</sup> *Institute of Thermal Physics, Ural Division, Russian Academy of Sciences, ul. Amundsena 106, GSP-828, Yekaterinburg, 620219 Russia*

<sup>b</sup> *Institute of Industrial Ecology, Ural Division, Russian Academy of Sciences, ul. S. Kovalevskoi 20a, GSP-594, Yekaterinburg, 620219 Russia*

Received June 20, 2006

**Abstract**—Vitreous and amorphous silicon nanoparticles composed of 500 atoms after a series of uniform tensions with a total strain  $\Delta l/l \approx 0.10$  and subsequent relaxation are investigated using the molecular dynamics method. The disappearance of the second peak in the radial distribution function for the amorphous nanoparticle subjected to a tensile strain  $\Delta l/l \approx 0.06$  indicates the destruction of a tetrahedral packing. In nanoparticles of both types, the energetically most favorable atomic packing is retained in middle layers at all the strains under investigation. The distribution of Si–Si bond lengths and a larger mean number of bonds per atom suggest that the structure of the vitreous nanoparticle is characterized by a higher statistic resistance to tension. This nanoparticle also has a higher kinetic resistance to uniform tension. Unlike the amorphous nanoparticle, the radial component of the coefficient of mobility of atoms in the vitreous nanoparticle is not dominant over its tangential component and does not increase regularly in going from the center of mass of the nanoparticle to the surface. As the number of tensions increases, the mean length of Si–Si bonds decreases in the vitreous nanoparticle and, by contrast, increases in the amorphous nanoparticle.

**DOI:** 10.1134/S1087659607020101

### INTRODUCTION

A progressively larger number of nanoparticle properties have come under the scrutiny of science in recent years. This can be explained by the following circumstances: (1) the necessity of knowing a variation in properties of materials when changing over from molecules to clusters, nanoparticles, and massive materials; (2) a qualitative improvement of experimental equipment intended for measuring and analyzing physical properties of nanoparticles; (3) an increasing role of nanoparticles in practical applications (catalysis, semiconductor magnetic devices); and (4) the use of nanoparticles as building blocks for preparing new solid materials or surface structures. The particular interest expressed by researchers in silicon nanoparticles is associated with the leading place of silicon in the fabrication of modern electronic products. However, a larger number of works have been devoted to investigation into the properties of small-sized silicon clusters ( $N \leq 45$ ) [1–4]. Meloni et al. [5] studied the anion photoelectron spectra of silicon clusters with  $N = 4–35$ . It was demonstrated that the transition from elongated to more spherical clusters should occur between  $N = 24$  and 28. Quantum Monte Carlo studies of  $\text{Si}_{20}$  and  $\text{Si}_{25}$  clusters revealed that the electronic correlation plays an important role in the stabilization of the isomer structure, the surface energy varies smoothly, and there are only one or two breakings of bonds for 0.1 ps [2]. The influence of external compressive forces on the formation of  $\text{SiO}_2$

nanoparticles containing 300 atoms was examined in the computer experiment performed in [6], and the effect of oxygen capture by a silicon nanoparticle growing to 302 atoms was studied in [7]. The structural and kinetic properties of a  $\text{Si}_{480}$  nanoparticle in the temperature range  $600 \text{ K} < T < 2000 \text{ K}$  were calculated by the molecular dynamics method with the use of the Stillinger–Weber potential [8]. In [8], the authors believed that the structure of the nanoparticle core is similar to the structure of massive vitreous silicon and that the self-diffusion coefficient of atoms in the nanoparticle at high temperatures is comparable to the self-diffusion coefficient of atoms in liquid silicon. The changeover to investigations into the properties of larger silicon structures is important from the standpoint of both microelectronics and development of methods for producing nonsintering spherical nanoparticles through chemical vapor deposition. Note that silicon nanoparticles deposited on a particular substrate or formed in the bulk of an  $\text{SiO}_2$  insulator can be subjected to large tensile strains.

In this work, we investigated the stability of noncrystalline silicon nanoparticles subjected to uniform tension, determined the dependence of their main physicochemical properties on the strain, and analyzed the influence of the method for preparing nanoparticles on their resistance to uniform tension.

## THE COMPUTER MODEL

The Si–Si interactions are described by the Stillinger–Weber potential represented as the sum of two functions  $\Phi_{(2)}$  and  $\Phi_{(3)}$  reflecting the contributions of two- and three-particle interactions [9]; that is,

$$\begin{aligned}\Phi_{(2)}(r_{ij}) &= \varepsilon f_{(2)}(r_{ij}/\sigma), \\ \Phi_{(3)}(\mathbf{r}_i, \mathbf{r}_j, \mathbf{r}_k) &= \varepsilon f_{(3)}(\mathbf{r}_i/\sigma, \mathbf{r}_j/\sigma, \mathbf{r}_k/\sigma),\end{aligned}\quad (1)$$

Here, the parameter  $\varepsilon$  is chosen so that  $f_{(2)} = -1$  at  $r_{ij} = \sigma$  and the parameter  $\sigma$  is chosen so that  $f_{(2)}(2^{1/6}) = 0$ . The quantity  $f_{(2)}$  is a function of a scalar, and the function  $f_{(3)}$  possesses a complete translational and vibrational symmetry. The contribution of pair interactions to the potential can be written in the form

$$f_{(2)}(r) = \begin{cases} A(Br^{-p} - r^{-q})e^{\frac{1}{r-a}}, & r < a, \\ 0 & r \geq a \end{cases}\quad (2)$$

where  $A$ ,  $B$ , and  $p$  are positive constants and  $q = 0$  for silicon.

The contribution of three-particle interactions can be represented as follows:

$$\begin{aligned}f_{(3)}(\mathbf{r}_i, \mathbf{r}_j, \mathbf{r}_k) &= h(\mathbf{r}_{ij}, \mathbf{r}_{ik}, \Theta_{jik}) + h(\mathbf{r}_{ji}, \mathbf{r}_{jk}, \Theta_{jik}) \\ &\quad + h(\mathbf{r}_{ki}, \mathbf{r}_{kj}, \Theta_{ikj}),\end{aligned}\quad (3)$$

Here,  $\Theta_{ijk}$  is the angle between the vectors  $\mathbf{r}_i$  and  $\mathbf{r}_k$  converging to the  $j$ th vertex. The function  $h$  is defined as

$$h(\mathbf{r}_{ij}, \mathbf{r}_{ik}, \Theta_{ijk}) = \begin{cases} \lambda e^{\frac{\gamma}{r_{ij}-a} + \frac{\gamma}{r_{ik}-a}} \left( \cos \Theta_{jik} + \frac{1}{3} \right), \\ r_{ij}, r_{ik} < a, \\ 0 & r \geq a \end{cases}\quad (4)$$

It is this parameter  $\Theta$  that provides information on the bond strains. The equality  $f_{(3)} = 0$  is satisfied for the perfect tetrahedral angle ( $\cos \Theta = -1/3$ ). All the parameters of potentials (1)–(4) are listed in the table. Compared to potentials based only on two-particle interactions, the Stillinger–Weber potential allows us to describe more accurately a set of strains. Figure 1 depicts the characteristics of the Stillinger–Weber potential in the form of the function  $\Phi_{(2)}$  representing the contribution of two-particle interactions and the dependence  $\Theta_{ijk}(r)$  (where  $r = r_{ij} = r_{kj}$ ) for five values of the three-particle contribution, namely, 8.67, 4.33, 2.17, 0.43, and 0.04 eV/atom. The curves depicted in Fig. 1 were calculated for silicon clusters containing from two to six atoms.

Numerical integration of the equations of motion was performed using the Verlet algorithm [10], which includes the direct calculations of particle velocities. This algorithm is one of the most stable algorithms, on the one hand, and makes it possible to control the temperature in the model with a sufficient accuracy, on the other hand. The time step  $\Delta t$  was equal to  $10^{-16}$  s.

## Parameters of the Stillinger–Weber potential [9]

Parameter	Value
$\varepsilon$ (eV)	2.16826
$A$	7.049556577
$B$	0.6022245584
$\sigma$ (nm)	0.20951
$p$	4
$q$	0
$a$	1.8
$\lambda$	21.0
$\gamma$	1.2

## COMPUTATIONAL TECHNIQUE

Silicon nanoparticles composed of 500 atoms were chosen as objects of simulation. Two types of  $\text{Si}_{500}$  nanoparticles with a noncrystalline atomic packing were obtained in our earlier work [11]. The first type is represented by a vitreous nanoparticle prepared by rapid cooling of a liquid silicon particle from a temperature of 3000 to 300 K. The second type is represented by an amorphous silicon nanoparticle whose initial configuration was produced by a random-number generator with subsequent structural relaxation at  $T = 300$  K. The influence of uniform tension on the physicochemical properties of the nanoparticles was investi-

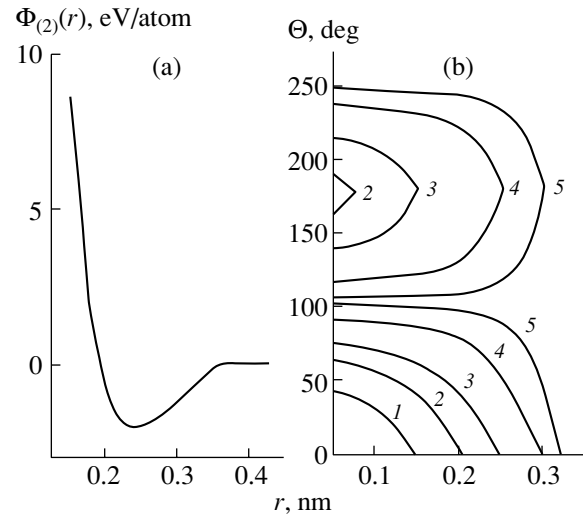


**Fig. 1.** Characteristics of the Stillinger–Weber potential: (a) the function  $\Phi_{(2)}(r)$  representing the contribution of the two-particle interactions and (b) the dependences of the angle  $\Theta$  with the vertex located at the center of the  $j$ th atom on the distance  $r = r_{ij} = r_{kj}$  to the centers of the  $i$ th and  $k$ th atoms forming this angle for three-particle contributions of (1) 8.67, (2) 4.33, (3) 2.17, (4) 0.43, and (5) 0.04 eV/atom. Isolines indicate three-particle contributions.

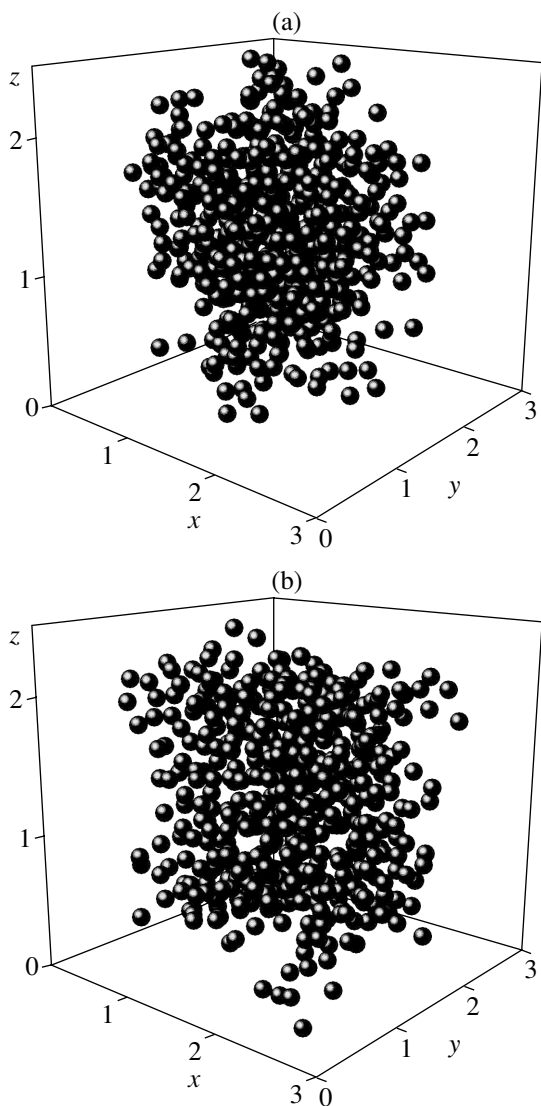


**Fig. 2.** Configurations of the (a) vitreous and (b) amorphous  $\text{Si}_{500}$  nanoparticles subjected to uniform tension at  $\Delta l/l \approx 0.10$ . The atomic coordinates are given in nanometers.

gated at a temperature of 300 K. The strain was specified by multiplying the coordinates of all atoms into a factor of 1.02. Then, the structural relaxation of the nanoparticle in this stretched state was simulated by molecular dynamics for  $10^6$  time steps  $\Delta t$ . The calculated final configuration of the nanoparticle was again strained by scaling at a factor of 1.02, and the structural relaxation was simulated by molecular dynamics for  $10^6$  time steps  $\Delta t$ . The scaling of the coordinates with subsequent structural relaxation was carried out seven

times, so that the total strain  $\sum_i^7 \Delta l_i/l_{i0}$  (where  $l_{i0}$  is the current characteristic length before relaxation) was approximately equal to 0.15. However, the real strain of the nanoparticles was considerably smaller due to the

structural relaxation (performed after tension), which led to a decrease in the nanoparticle volume. Hereafter, all the results under consideration will be considered with the total strain that takes into account the relaxation and, for brevity, will be designated as  $\Delta l/l$ . The maximum strain ( $\Delta l/l \approx 0.10$ ) observed for the nanoparticles after structural relaxation corresponds to the total strain of a surface silicon layer implanted with erbium ions at energies of 0.8–2.0 MeV [12]. Figure 2 shows the configurations of the vitreous and amorphous silicon nanoparticles formed as a result of the structural relaxation after a number of sequential uniform tensions with the total strain  $\Delta l/l = 0.10$ . The density of the central region of both nanoparticles is higher than that of their peripheral regions. The radial density gradient in the vitreous nanoparticle is higher than that in the amorphous nanoparticle.

The physicochemical characteristics of the nanoparticles were calculated at time intervals equal to  $10^6 \Delta t$ , which were defined as the structural relaxation periods. The mean length of Si–Si bonds  $\langle L_b \rangle$  and the mean number of bonds  $\langle n_b \rangle$  per atom were determined by constructing Voronoi polyhedra after each thousand of time steps. Among the nearest neighbors revealed using the Voronoi polyhedra, the nearest neighbors located at a distance of no more than 0.3 nm were taken into account. A distance of 0.3 nm is close to the parameter in the Morse potential describing the Si–Si interactions [13]. This made it possible to determine the bond lengths  $L_b$  and the numbers  $n_b$  of bonds. In order to study thoroughly the physicochemical properties of the nanoparticles, their volume was approximated by a sphere divided into concentric layers of identical thickness  $d$ . The sphere whose radius was four times larger than the thickness  $d$  was treated as the first layer. The centers of spheres and concentric layers coincided with the center of mass of the nanoparticles. The number of atoms in each spherical layer was determined every  $10 \Delta t$ . The potential energies and the coefficients of mobility of atoms in each layer were calculated at the same time intervals. The mean number of atoms in the first layer was equal to 19 in the vitreous nanoparticle and 11 in the amorphous nanoparticle. The difference between the numbers of atoms in other layers was no more than 40. More detailed information on the layer state can be obtained from the relative excess potential energy, which is defined by the relationship

$$\Delta U/\langle U \rangle = (U_n - \langle U \rangle)/\langle U \rangle, \quad (5)$$

where  $U_n$  is the potential energy of the atoms forming the  $n$ th layer and  $\langle U \rangle$  is the mean potential energy of the nanoparticle. The layers were numbered beginning from the center of the nanoparticle.

The total coefficient of mobility of atoms was calculated through the mean square of atomic displacement according to the expression [13]

$$D = \lim_{t \rightarrow \infty} \frac{1}{6t} \frac{1}{N} \sum_{i=1}^N [\mathbf{r}_i(t+t_0) - \mathbf{r}_i(t_0)]^2, \quad (6)$$

where  $\mathbf{r}_i(t)$  is the radius vector of the  $i$ th atom at the instant of time  $t$  and  $t_0$  is the initial instant of time. The atomic displacements in a spherical cluster are represented by two components: the radial component  $\langle(\Delta\mathbf{r})^2\rangle_r$ , characterizes the atomic displacement toward the center of the cluster (or in the opposite direction), and the tangential component  $\langle(\Delta\mathbf{r})^2\rangle_t$ , corresponds to the atomic displacements in the directions perpendicular to the radial direction. These components are written in the form

$$D_r = \frac{1}{6} \lim_{t \rightarrow \infty} \frac{\langle r^2(t+t_0) + r^2(t_0) - 2r(t+t_0)r(t_0) \rangle}{t}, \quad (7)$$

$$D_t = \frac{1}{6} \lim_{t \rightarrow \infty} \frac{\langle r(t+t_0)r(t_0)[2 - 2\mathbf{u}(t+t_0)\mathbf{u}(t_0)] \rangle}{t}, \quad (8)$$

where  $\mathbf{u} = \mathbf{r}(t)/|\mathbf{r}(t)|$  is the unit vector and  $D$ ,  $D_r$ , and  $D_t$  stand for the coefficients of mobility of atoms in the nanoparticles. We calculated the radial distributions of these quantities averaged over the concentric layers of the spherical cluster. Since the equality  $\langle(\Delta\mathbf{r})^2\rangle = \langle(\Delta\mathbf{r})^2\rangle_r + \langle(\Delta\mathbf{r})^2\rangle_t$  holds true, the coefficients of mobility are related by the expression  $D = D_r + D_t$ .

## RESULTS OF CALCULATIONS

An increase in the potential energy of the studied nanoparticles under the strains does not exceed 6%. At the strain  $\Delta l/l = 0.10$ , the potential energies of the vitreous and amorphous  $\text{Si}_{500}$  nanoparticles are equal to  $-3.6$  and  $-3.2$  eV/atom, respectively. These potential energies are in agreement with the potential energy ( $-3.48$  eV/atom) of the vitreous nanoparticle consisting of 480 atoms [8]. The excess potential energies for the concentric layers of the  $\text{Si}_{500}$  amorphous nanoparticle are depicted in Fig. 3. It can be seen from this figure that the potential energies  $U$  of the five layers nearest to the center of mass of the nanoparticle and six outer layers are higher than the mean potential energy  $\langle U \rangle$  of the nanoparticle. The potential energies of the middle layers (from sixth to ninth) are lower than the mean potential energy  $\langle U \rangle$ . An increase in the tensile strain of the nanoparticle results in a decrease in the excess potential energy of the seventh and eighth layers and an increase in the corresponding energy of the second to fifth layers. For the  $\text{Si}_{500}$  vitreous nanoparticle, an increase in the strain leads to a decrease in the excess potential energy  $\Delta U$  of the sixth to ninth layers. In this case, the sixth concentric layer has the lowest potential energy. Note that, already at the strain  $\Delta l/l = 0.06$ , the potential

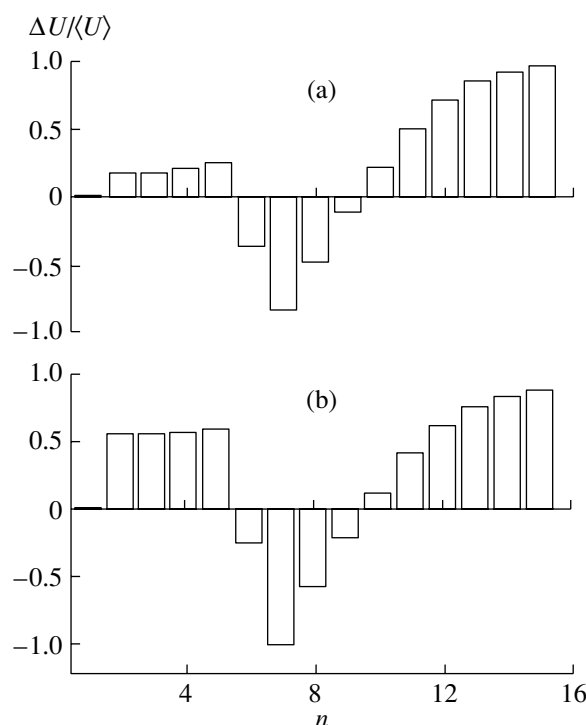


**Fig. 3.** Excess potential energies of the concentric layers in the  $\text{Si}_{500}$  amorphous nanoparticle subjected to uniform tension at  $\Delta l/l =$  (a) 0.03 and (b) 0.10. Spherical layers are labeled with numbers  $n$  beginning from the center of the nanoparticle to the surface.

energy of the sixth layer is 100% lower than the mean potential energy of the nanoparticle. As the strain increases, the number of energetically favorable layers with  $U_n < \langle U \rangle$  increases neither in the vitreous nanoparticle nor in the amorphous nanoparticle.

The radial distribution function constructed for the atom nearest to the center of mass of the  $\text{Si}_{500}$  amorphous nanoparticle is shown in Fig. 4. At small tensile strains ( $\Delta l/l \approx 0.03$ ), the function  $g(r)$  exhibits two peaks. The presence of the second peak in this function indicates the formation of the second coordination layer, i.e., an increase in the short-range order region. The function  $g(r)$  for the  $\text{Si}_{500}$  amorphous nanoparticle at  $\Delta l/l \approx 0.03$  and the radial distribution function for the massive glass simulated by molecular dynamics [15] are compared in Fig. 4a. The first peak in the function  $g(r)$  for the strained nanoparticle is shifted toward longer distances as compared to that for the silicon glass simulated by molecular dynamics. By contrast, the second peak in the former function is shifted toward the shorter distances. The short-range order in the stretched nanoparticle differs from the local order in the massive glass. At tensile strains  $\Delta l/l \geq 0.06$ , the second peak in the radial distribution function transforms into a shoulder. Therefore, large tensile strains lead to a decrease in the short-range order region and to a less ordered atomic packing in the amorphous nanoparticle.

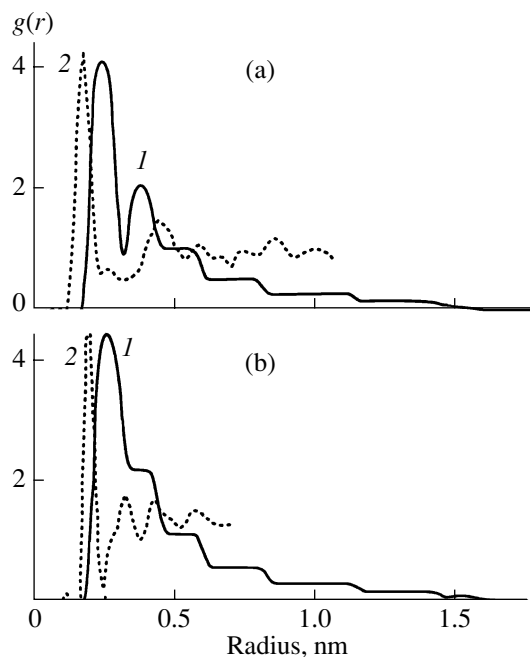


**Fig. 4.** Radial distribution functions for (1) the  $\text{Si}_{500}$  amorphous nanoparticle subjected to uniform tension at  $\Delta l/l =$  (a) 0.03 and (b) 0.06, (a) (2) the massive silicon glass simulated by molecular dynamics [15], and (b) (2) the random hard-sphere model involving 35% of holes [16].

The function  $g(r)$  for the  $\text{Si}_{500}$  amorphous nanoparticle at  $\Delta l/l \approx 0.06$  and the corresponding function obtained within the random hard-sphere model involving 35% of holes [16] are compared in Fig. 4b. In the hard-sphere model, the function  $g(r)$  was constructed under the assumption that the hard-sphere diameter is equal to the parameter  $\sigma$  of the Stillinger–Weber potential. In the presence of holes in the random hard-sphere model, the peaks in the radial distribution function decrease in intensity and become broader. The main peak in the radial distribution function for the stretched nanoparticle is shifted toward the right with respect to the first peak in the function  $g(r)$  for the random hard-sphere model. The tails of the functions  $g(r)$  for the vitreous silicon nanoparticle and the random hard-sphere model also differ substantially. This suggests that the structure of the amorphous silicon nanoparticle differs significantly from the random packing of hard spheres with random holes. The second peak in the function  $g(r)$  for the  $\text{Si}_{500}$  vitreous nanoparticle is retained at all the tensile strains used. This means that the tension does not result in a considerable change in the short-range order and, hence, the vitreous nanoparticle has a higher strength with respect to the uniform tension strain.

The radial density profiles for the nanoparticles at  $\Delta l/l = 0$  and 0.10 are depicted in Fig. 5. The profiles were constructed for the atom nearest to the center of mass of the nanoparticle. For the unstrained nanoparti-

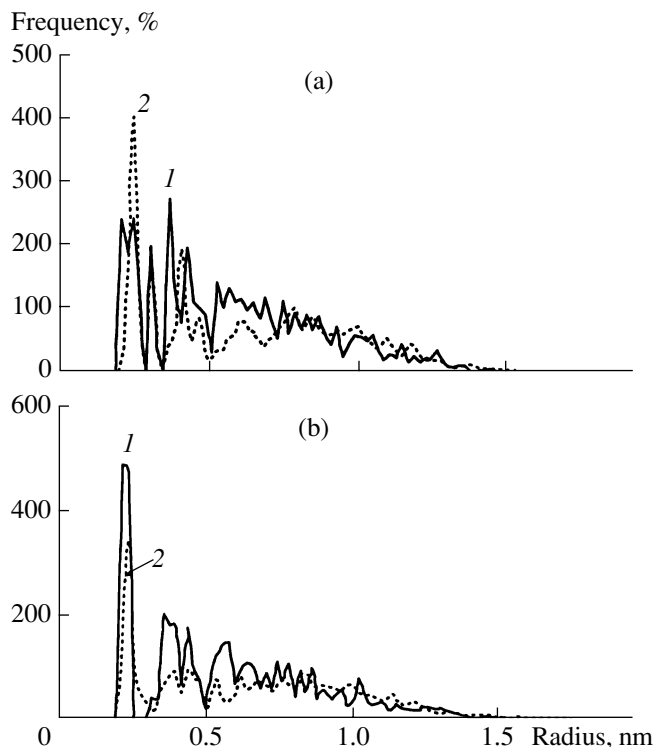


**Fig. 5.** Radial density profiles for the (1) vitreous and (2) amorphous  $\text{Si}_{500}$  nanoparticles at strains  $\Delta l/l =$  (a) 0.00 and (b) 0.10.

cles, the amorphous nanoparticle has the highest density observed at  $r = 0.24$  nm. For the vitreous nanoparticle, the most intense peak occurs at  $r = 0.36$  nm. The situation changes radically for the stretched nanoparticles. At a strain  $\Delta l/l \approx 0.10$ , the main peak in the radial density distribution is shifted to 0.22 nm for the vitreous nanoparticle and, as before, is located at 0.24 nm for the amorphous nanoparticle. In this case, the intensity of the main peak in the radial density distribution for the vitreous nanoparticle is higher than that for the amorphous nanoparticle.

The unstrained vitreous nanoparticle has a more homogeneous structure, which is similar in many respects to the structure of the massive silicon glass. The construction of Voronoi polyhedra permits us to analyze the angles  $\theta$  of the mutual arrangement of neighboring atoms in the nanoparticles. The angle  $\theta$  is defined as an angle whose vertex is located at the center of the Voronoi polyhedron that coincides with the center of mass of a cluster. The sides of this angle pass through the centers of atoms that form the polyhedron faces. The faces of Voronoi polyhedra determine the nearest geometric neighbors. The angular distribution of the nearest geometric neighbors in the  $\text{Si}_{500}$  initial vitreous nanoparticle exhibits two peaks whose maxima are located at  $63^\circ$  and  $105^\circ$  (Fig. 6a). The corresponding angular distribution for the  $\text{Si}_{500}$  amorphous nanoparticle contains three peaks with maxima at  $42^\circ$ ,

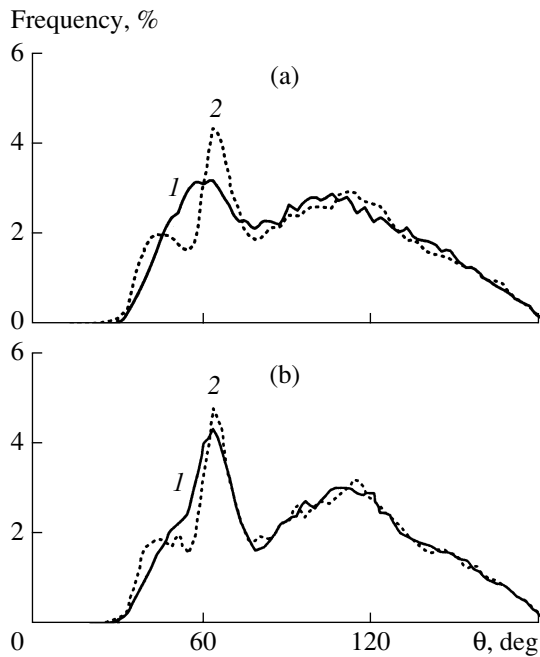


**Fig. 6.** Angular distributions of the nearest geometric neighbors in the (1) vitreous and (2) amorphous  $\text{Si}_{500}$  nanoparticles at tensile strains  $\Delta l/l =$  (a) 0.00 and (b) 0.10.

$63^\circ$ , and  $111^\circ$ . The uniform tension leads to a change in the distributions of  $\theta$  angles. As before, the angular distribution involves two peaks for the vitreous nanoparticle and three peaks for the amorphous nanoparticle. Under tension at a strain  $\Delta l/l \approx 0.10$ , the location of the first peak in the distribution of  $\theta$  angles in the vitreous nanoparticle remains unchanged, whereas the maximum of the second peak is shifted toward the right to  $111^\circ$  (Fig. 6b). In this case, the height of the first peak increases by 47% and the height of the second peak decreases by 7%. Under the same strain of the amorphous nanoparticle, the maximum of the first peak in the angular distribution is shifted to  $51^\circ$ , the location of the maximum of the second peak remains unchanged, and the maximum of the third peak is shifted to  $114^\circ$ . In this case, the height of the first peak decreases by 0.6% and the heights of the second and third peaks increase by 9.0 and 6.0%, respectively.

The distributions of Si–Si bond lengths in the vitreous and amorphous  $\text{Si}_{500}$  nanoparticles at  $\Delta l/l = 0.00$  and  $\approx 0.10$  are depicted in Fig. 7. The unstrained vitreous nanoparticle is characterized by a broad distribution of bond lengths with five low-intensity maxima and four shallow minima. The first two most intense maxima correspond to bond lengths of 0.215 and 0.235 nm. The distribution of the bond lengths  $L_b$  for the initial amorphous nanoparticle exhibits a main peak at 0.235 nm and a weak peak at 0.261 nm. The uniform tension strain leads to a substantial change in the distribution of bond lengths  $L_b$  for both nanoparticles. At a

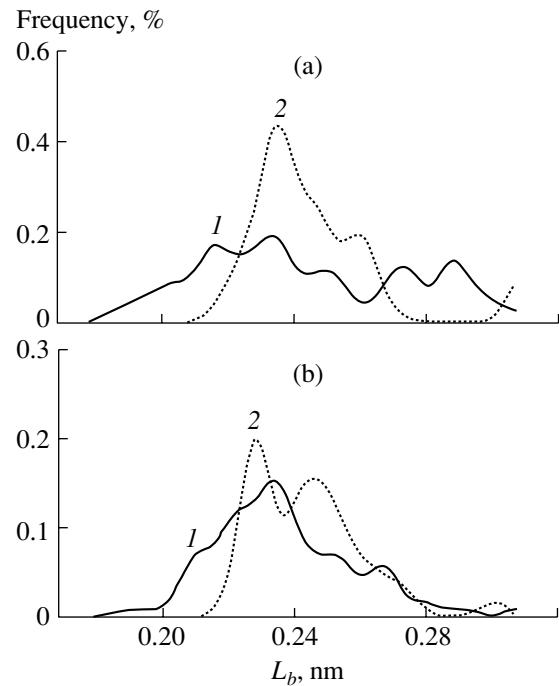


**Fig. 7.** Distributions of Si–Si bond lengths in the (1) vitreous and (2) amorphous  $\text{Si}_{500}$  nanoparticles at tensile strains  $\Delta l/l =$  (a) 0.00 and (b) 0.10.

strain  $\Delta l/l \approx 0.10$ , the distribution of bond lengths for the vitreous becomes unimodal with a maximum at 0.235 nm and a weak peak at 0.267 nm. The corresponding distribution for the amorphous nanoparticle is bimodal with maxima at 0.228 and 0.248 nm. In the absence of strains, the mean length  $\langle L_b \rangle$  of Si–Si bonds in the vitreous nanoparticle is somewhat larger than that in the amorphous nanoparticle (Fig. 8a). However, the mean lengths  $\langle L_b \rangle$  in the nanoparticles under investigation level off even under tension with a strain  $\Delta l/l \approx 0.007$ . With a further increase in the strain, the mean length  $\langle L_b \rangle$  in the vitreous nanoparticle becomes considerably smaller than that in the amorphous nanoparticle. At any strain, the mean number of bonds per atom in the vitreous nanoparticle is larger than that in the amorphous nanoparticle (Fig. 8b). Note that the maximum value of  $\langle n_b \rangle$  corresponds to a strain  $\Delta l/l \approx 0.052$  for the vitreous nanoparticle and  $\approx 0.10$  for the amorphous nanoparticle.

The radial  $D_r$  and tangential  $D_t$  components of the coefficient  $D$  of mobility of atoms in the initial amorphous nanoparticle are close to each other, whereas the tangential component is considerably larger than the radial component for the vitreous nanoparticle. The uniform tension of the nanoparticles leads to the redistribution of the radial component of the coefficient of mobility  $D$  between the spherical layers, so that the radial component  $D_r$  of the coefficient of mobility decreases for the layers nearest to the center of mass of the nanoparticle and increases for the outer layers. The

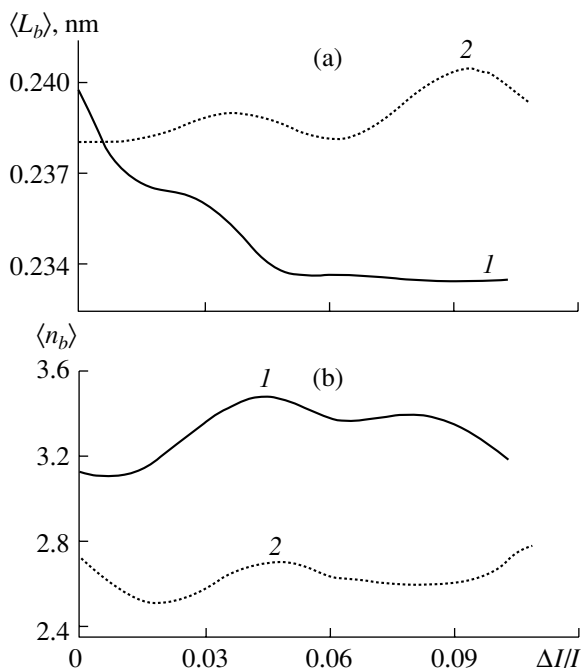


**Fig. 8.** Dependences of (a) the mean length of Si-Si bonds and (b) the mean number of bonds per atom on the strain  $\Delta/l$  for the (1) vitreous and (2) amorphous  $\text{Si}_{500}$  nanoparticles.

corresponding changes are pronounced for the amorphous nanoparticle and are rather insignificant for the vitreous nanoparticle (Fig. 9).

## DISCUSSION OF THE RESULTS

The computer simulation indicates that the potential energy is characterized by a nonuniform distribution over concentric layers of the nanoparticles. The energetically most favorable packing occurs in the middle spherical layers of the nanoparticles. Note that, in the vitreous nanoparticle, the layer with the lowest potential energy borders the layer whose energy is higher than the mean potential energy of the nanoparticle. In the amorphous nanoparticle, the layer with the minimum potential energy is surrounded by the layers whose energy is lower than the mean potential energy  $\langle U \rangle$  of the nanoparticle. Therefore, compared to the state of the amorphous nanoparticle, the state of the vitreous nanoparticle turns out to be more energetically strained. The distribution of Si-Si bond lengths in the unstrained vitreous nanoparticle is considerably more uniform and becomes similar to a normal distribution after a series of uniform tensions. The final distribution for the vitreous nanoparticle has a maximum at the bond length  $L_b = 0.235$  nm, which is equal to the length of Si-Si bonds in crystalline silicon. The short-range order in the amorphous nanoparticle strained at  $\Delta/l \approx$

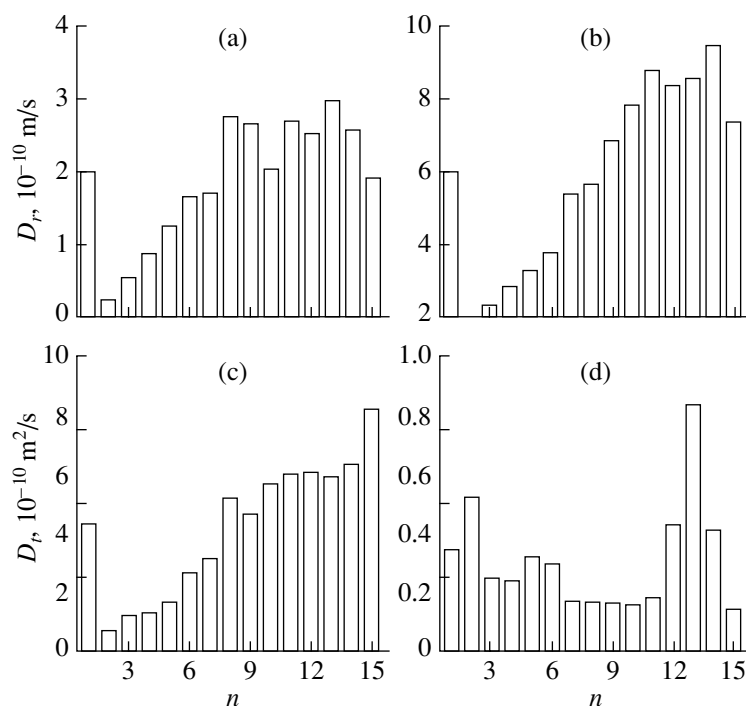


**Fig. 9.** (a, b) Radial and (c, d) tangential components of the coefficient  $D$  of mobility of atoms in concentric layers of the (a, c) vitreous and (b, d) amorphous  $\text{Si}_{500}$  nanoparticles.

0.10 is governed by the two most favorable bond lengths  $L_b$ , none of which corresponds to the bond length  $L_b$  in crystalline silicon. A higher ordering of the structure of the strained vitreous nanoparticle is also evidenced by the retention of the second peak in the function  $g(r)$  after all strains. Note that this peak in the function  $g(r)$  for the amorphous nanoparticle disappears under tension at  $\Delta l/l \approx 0.06$ . The presence of the second peak in the function  $g(r)$  suggests that atoms in the nanoparticles have a tetrahedral coordination. For the tetrahedral coordination, the short-range order is determined by the two coordination spheres, as is the case with the diamond lattice [17]. However, rotation of tetrahedra about the bond joining them together leads to a change in the distance to the third neighbors. Therefore, the third peak in the function  $g(r)$  disappears when changing over from crystalline to noncrystalline silicon. The disappearance of the second peak for the highly strained amorphous nanoparticle can be attributed to the disappearance of the tetrahedral ordering of atoms. The radial density profile for the vitreous nanoparticle strained at  $\Delta l/l \approx 0.10$  exhibits the highest peak at  $r = 0.24$  nm, whereas the same peak is dominant in the radial density profile for the initial amorphous nanoparticle. The amorphous nanoparticle has a more complex angular distribution of the nearest geometric neighbors. However, as the strain of this nanoparticle increases, the first peak in the distribution of angles  $\theta$  becomes more poorly resolved. The angular distribution of the nearest neighbors for the vitreous nanoparticle is similar to the corresponding distribution for a simple frozen liquid. Note that, as the nanoparticle strain increases, the resolution of the peaks is improved, i.e., the orientational ordering becomes more pronounced. The vitreous and amorphous nanoparticles have a similar topological disordering. For both nanoparticles, dodecahedra are dominant in the distributions of Voronoi polyhedra over the number of faces after eliminating small-sized sides with lengths  $l < 0.5\bar{l}$  (where  $\bar{l}$  is the mean length of sides in Voronoi polyhedra) and pentagons are dominant in the distributions of faces over the number of sides. Irrespective of the strain, a larger fraction of six-membered rings and a smaller fraction of four-membered cyclic structures in the vitreous nanoparticle are the most significant topological difference between the structures of the vitreous and amorphous nanoparticles.

### CONCLUSIONS

Thus, the results of the performed investigation demonstrated that the physicochemical properties of silicon nanoparticles subjected to strain depend on the method for preparing these nanoparticles. Consequently, a particular technique for producing nanomaterials should be chosen depending on the field of application. As the strain increases, the mean bond length decreases for the vitreous nanoparticle and somewhat

increases for the amorphous nanoparticle. The number of bonds per atom in the vitreous nanoparticle at the strains under investigation is larger than that in the amorphous nanoparticle. Consequently, vitreous nanoparticles should be more brittle, whereas amorphous nanoparticles should be more prone to tension. An approximate static criterion for the stability of amorphous and vitreous silicon nanoparticles with respect to the formation of crystalline or liquid phases can serve an increase in the intensity of the first peak in the function  $g(r)$  by more than 10% as compared to the intensity of this peak at room temperature. However, a more accurate indication of the onset of transformation is provided by the kinetic criterion of the stability according to which a nanoparticle acquires "fluidity" when atomic displacements in the radial direction predominate over atomic displacements in the tangential direction. Compared to amorphous nanoparticles, vitreous nanoparticles with a similar size are characterized by a considerably larger tangential component and a smaller radial component of the coefficient of mobility of atoms. Unlike the amorphous nanoparticle, the radial component  $D_r$  of the coefficient of mobility of atoms in the vitreous nanoparticle does not increase progressively in going from the inner concentric layers to the outer layers even at large tensile strains ( $\Delta l/l \approx 0.10$ ).

Therefore, the strength of noncrystalline silicon nanoparticles depends on the procedure of their preparation. The vitreous nanoparticle subjected to tensile strain appears to be more brittle than the amorphous nanoparticle that have identical size and is subjected to the same tensile strain.

### ACKNOWLEDGMENTS

This study was supported by the Presidium of the Ural Division of the Russian Academy of Sciences within the framework of the Integration Project of the Ural Division–Far East Division of the Russian Academy of Sciences.

### REFERENCES

1. Ho, K.M., Shvartsburg, A.A., Pan, B., *et al.*, Structures of Medium-Sized Silicon Cluster, *Nature*, 1998, vol. 392, no. 6676, pp. 582–585.
2. Mitas, L., Grossman, J.C., Stock, I., and Tobic, J., Silicon Clusters of Intermediate Size: Energetics, Dynamics, and Thermal Effects, *Phys. Rev. Lett.*, 2000, vol. 84, no. 7, pp. 1479–1482.
3. Dai, D. and Balasubramanian, K., Geometries and Energy Separations of the Electronic States of  $\text{Ge}_5^+$  and  $\text{Sn}_5^+$ , *J. Chem. Phys.*, 1998, vol. 108, no. 11, pp. 4379–4385.
4. Sieck, A., Porezad, D., Frauenheim, T., *et al.*, Structure and Vibrational Spectra of Low-Energy Silicon Clusters, *Phys. Rev. A: At., Mol., Opt. Phys.*, 1997, vol. 56, no. 6, pp. 4890–4898.

5. Meloni, G., Ferguson, M.J., Sheehal, S.M., and Neumarck, D.M., Probing Structural Transitions of Nanosize Silicon Cluster via Anion Photoelectron Spectroscopy at 7.9 eV, *Chem. Phys. Lett.*, 2004, vol. 399, no. 4, pp. 389–391.
6. Galashev, A.E. and Skokov, V.N., The Nucleation of a Nanoparticle of Silicon Dioxide in a Closed Domain. Computer Experiment, *Teplofiz. Vys. Temp.*, 2003, vol. 41, no. 3, pp. 386–394 [*High Temp.* (Engl. transl.), 2003, vol. 41, no. 3, pp. 327–331].
7. Galashev, A.E., Growth of a Si Nanocrystal in an Oxygen Atmosphere. Computer Simulation, *Kristallografiya*, 2002, vol. 47, no. 2, pp. 169–176 [*Crystallogr. Rep.* (Engl. transl.), 2002, vol. 47(Suppl. 1), pp. 169–176].
8. Zachariah, M.R., Carrier, M.J., and Blaisten-Barojas, E., Properties of Silicon Nanoparticles: A Molecular Dynamics Study, *J. Phys. Chem.*, 1996, vol. 100, no. 36, pp. 14856–14864.
9. Stillinger, F.H. and Weber, T.A., Computer Simulation of Local Order in Condensed Phases of Silicon, *Phys. Rev. B: Condens. Matter*, 1985, vol. 31, no. 8, pp. 5262–5271.
10. Verlet, L., Computer “Experiments” on Classical Fluids: 1. Thermodynamical Properties of Lennard-Jones Molecules, *Phys. Rev.*, 1967, vol. 159, no. 1, pp. 98–103.
11. Galashev, A.E., Polukhin, V.A., Izmodenov, I.A., and Galasheva, O.A., Computer Simulation of the Structure of Vitreous and Amorphous Silicon Nanoparticles, *Poverkhnost*, 2006, no. 1, pp. 41–49.
12. Kyutt, R.N. and Sobolev, N.A., X-ray Diffraction Studies of Silicon Implanted with High-Energy Erbium Ions, *Fiz. Tverd. Tela* (St. Petersburg), 1997, vol. 39, no. 5, pp. 853–857 [*Phys. Solid State* (Engl. transl.), 1997, vol. 39, no. 5, pp. 759–762].
13. Kubicki, J.D. and Lasaga, A.C., Molecular Dynamics Simulations of SiO<sub>2</sub> Melt and Glass: Ionic and Covalent Models, *Am. Mineral.*, 1988, vol. 73, no. 9, pp. 941–955.
14. Briant, C.L. and Burton, J.J., Melting of a Small Cluster of Atoms, *Nature: Phys. Sci.*, 1973, vol. 243, no. 11, pp. 100–102.
15. Biswas, R., Grest, G.S., and Soukoulis, C.M., Generation of Amorphous-Silicon Structures with Use of Molecular-Dynamics Simulations, *Phys. Rev. B: Condens. Matter*, 1987, vol. 36, no. 15, pp. 7437–7441.
16. Bernal, J.D. and King, S.V., Experimental Modeling of Simple Liquids, in *Physics of Simple Liquids*, Temperley, H.N.V., Rowlinson, J.S., and Rushbrooke, G.S., Eds., Amsterdam: North-Holland, 1968. Translated under the title *Fizika prostykh zhidkostei*, Moscow: Mir, 1971.
17. Ziman, J.M., *Models of Disorder: The Theoretical Physics of Homogeneously Disordered Systems*, Cambridge: Cambridge Univ. Press, 1979. Translated under the title *Modeli besporyadka. Teoreticheskaya fizika odnorodno neuporyadochennykh sistem*, Moscow: Mir, 1982.

SPELL: OK